



Cobalt nanoparticles-encapsulated holey nitrogen-doped carbon nanotubes for stable and efficient oxygen reduction and evolution reactions in rechargeable Zn-air batteries

Eun Yeop Choi^{a,b,*}, Dong Eun Kim^a, Seung Youn Lee^a, Chul B. Park^b, Chang Keun Kim^{a,**}

^a School of Chemical Engineering & Materials Science, Chung-Ang University, 221 Huksuk-dong, Dongjak-gu, Seoul 156-756, South Korea

^b Microcellular Plastics Manufacturing Laboratory, Department of Mechanical & Industrial Engineering, University of Toronto, 5 King's College Rd, Toronto, Ontario M5S 3G8, Canada

ARTICLE INFO

Keywords:

Cobalt nanoparticle
Holey carbon nanotube
Electrocatalyst
Zn-air battery

ABSTRACT

A new, simple, and inexpensive approach for fabricating electrocatalysts is developed to optimize oxygen reduction reaction (ORR) and oxygen evolution reaction (OER) efficiency rechargeable Zn-air batteries. Holey N-doped carbon nanotubes (H-NCNT) are prepared by a simple reaction, and then Co nanoparticles are encapsulated inside the H-NCNT (Co@H-NCNT) through the holes of the H-NCNT. Electrocatalytic activities of Co@H-NCNT toward ORR and OER are explored, and comparable to those of the Pt/C and IrO₂. This is because the core-shell microstructure of Co@H-NCNT effectively forms catalytic active sites. Density functional theory (DFT) calculation reveals that the active sites in Co@H-NCNT have low overpotentials for ORR and OER, resulting in excellent catalytic activities. A Zn-air battery using Co@H-NCNT exhibits excellent power density (207.0 mW/cm²) and stability after 300 cycles. Therefore, Co@H-NCNT is a promising bi-functional ORR and OER catalyst for efficient electrocatalysis in Zn-air batteries with superior energy capacity and cycle durability.

1. Introduction

Energy crises and environmental concerns caused by the rapid consumption of fossil fuels have led to an urgent demand for the development of new and eco-friendly energy technologies. In recent years, rechargeable Li-ion battery markets have grown significantly, owing to the development of eco-friendly electric vehicles. However, Li-ion batteries have limited energy density, high cost, and safety issues, and thus the wide adoption of electric vehicles in the market still faces significant hurdles. After the Li-ion battery technologies, rechargeable Zn-air batteries have attracted significant interest due to their high theoretical energy density (1084 Wh/kg), abundant availability, and safety [1–12]. However, commercial applications of rechargeable Zn-air batteries have several disadvantages such as lower energy density than the theoretical value and poor cycling stability [3,10].

The technical issues hindering the commercialization of Zn-air

batteries mainly include slow oxygen reduction reaction (ORR) and oxygen evolution reaction (OER) kinetics at the air cathode [4,5]. Precious metal catalysts based on Pt, Ru and Ir have been explored to reduce the ORR and OER overpotentials for accelerating the reaction kinetics [13–17]. Although these materials have good catalytic activity, their high cost and low durability in ORR and OER conditions have impeded the commercial application of Zn-air batteries [2,4,13]. Therefore, the development of efficient and cheap catalyst for oxygen electrocatalysis in Zn-air batteries remains a major challenge.

Non-precious metal catalysts have received significant attention in oxygen electrocatalysis owing to their abundant availability and low cost. Specifically, transition metals (M = Fe, Co, Ni, etc.) integrated with nitrogen-doped carbons (M/N-C) are regarded as the promising alternatives to precious metal catalysts owing to their outstanding bi-functional ORR and OER activities [18–48]. Among the various microstructures for M/N-C catalysts, N-doped carbons encapsulating

Abbreviations: H-NCNT, Holey N-doped carbon nanotube; Co@H-NCNT, Co nanoparticles-encapsulated H-NCNT; ORR, oxygen reduction reaction; OER, oxygen evolution reaction.

* Corresponding author at: School of Chemical Engineering & Materials Science, Chung-Ang University, 221 Huksuk-dong, Dongjak-gu, Seoul 156-756, South Korea.

** Corresponding author.

E-mail addresses: eychoi1172@gmail.com (E.Y. Choi), ckkim@cau.ac.kr (C.K. Kim).

<https://doi.org/10.1016/j.apcatb.2023.122386>

Received 30 September 2022; Received in revised form 21 December 2022; Accepted 5 January 2023

Available online 6 January 2023

0926-3373/© 2023 Elsevier B.V. All rights reserved.

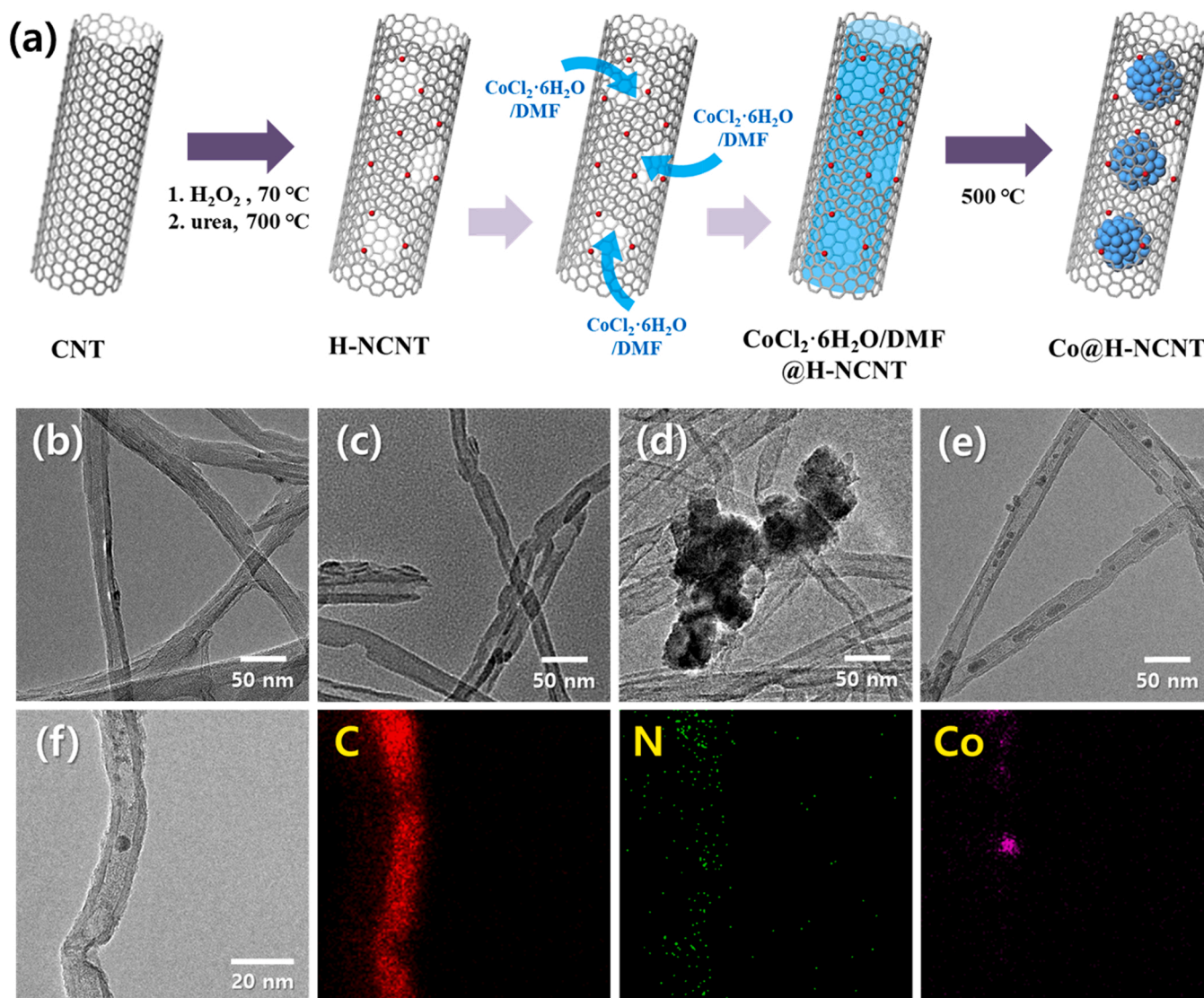


Fig. 1. (a) Schematic illustration for the fabrication of Co@H-NCNT, HR-TEM photographs of (b) pristine MWCNT, (c) H-NCNT, (d) Co/H-NCNT, (e) Co@H-NCNT, and (f) EDS mapping of Co@H-NCNT.

transition metal particles (M@N-C) have high electrocatalytic activity as well as long-term durability [19–22,25,31–34,39–42]. Core-shell microstructures of M@N-C can effectively prevent the degradation of metal particles by the electrolyte, resulting in M@N-C having high durability in ORR and OER conditions. For instance, bamboo-like carbon nanotube/Fe₃C nanoparticle hybrids exhibited M@N-C microstructure and superior ORR activity [19]. Cobalt-iron carbides encapsulated in N-doped graphene exhibited high durability in ORR conditions [22]. Co₉S₈ particles-encapsulated N-doped porous carbons showed bifunctional ORR and OER activities and outstanding durability [26]. Co encapsulated N-doped graphene exhibited good ORR and OER performances in both alkaline and seawater [32]. Bimetallic Co and Fe nanoparticles embedded in N-doped hollow carbon nanospheres were examined as electrocatalysts for Zn-air batteries and exhibited superior catalytic durability [39]. N-doped hollow carbon nanofibers encapsulating Co nanoparticles exhibited outstanding ORR and OER activities and high power density in Zn-air battery [42]. Although these M@N-C catalysts exhibited superior performances in ORR and OER, the synthesis of M@N-C catalysts requires expensive precursors and sophisticated control of the reaction conditions, which hinders their commercial application. Furthermore, their performances in Zn-air batteries remains insufficient, such as charge-discharge cycling stability. Therefore, a new

and simple method is required for the fabrication of M@N-C catalysts for developing non-precious and highly active electrocatalysts for Zn-air batteries.

In our previous study, we developed holey N-doped carbon nanotubes (H-NCNT), which have numerous holes on their sidewalls [49]. The holey structure of H-NCNT facilitates the penetration of metal precursors, making it easy to encapsulate metal particles in the H-NCNT. In this study, a new M@N-C catalyst with a distinct structure, cobalt nanoparticles-encapsulated H-NCNT (Co@H-NCNT), was fabricated and examined as an effective bi-functional ORR and OER catalyst for rechargeable Zn-air battery. The electrocatalytic activities of Co@H-NCNT toward ORR and OER were compared with those of a mixture of Co nanoparticles and H-NCNT (Co/H-NCNT) to prove the advantage of the M@N-C microstructure. Fe nanoparticles-encapsulated H-NCNT (Fe@H-NCNT) and Ni nanoparticles-encapsulated H-NCNT (Ni@H-NCNT) were fabricated, and their performance in Zn-air batteries was evaluated to compared with that of Co@H-NCNT. Further, density functional theory (DFT) calculation was performed for Fe@H-NCNT, Ni@H-NCNT, and Co@H-NCNT to confirm the possible active sites and compare their electrocatalytic activities.

2. Experimental section

2.1. Materials

Multi-walled carbon nanotubes (MWCNT, diameter: 15–20 nm, average length: 1.6 μm) were purchased from Hanwha Nanotech Co. (Seoul, Korea). Dimethylformamide (DMF), hydrogen peroxide (H_2O_2), and urea purchased from Sigma Aldrich (Milwaukee, WI, USA) were used for the preparation of H-NCNT. Cobalt (II) chloride hexahydrate ($\text{CoCl}_2 \cdot 6 \text{H}_2\text{O}$), iron (III) chloride hexahydrate ($\text{FeCl}_3 \cdot 6 \text{H}_2\text{O}$), and nickel (II) chloride hexahydrate ($\text{NiCl}_2 \cdot 6 \text{H}_2\text{O}$) were purchased from Sigma Aldrich and used as precursors for the formation of transition metal nanoparticles. Iridium oxide (IrO_2) and Pt nanoparticles deposited on carbon (Pt/C) were purchased from Alfa Aesar (Ward Hill, MA, USA).

2.2. Fabrication of catalysts

Synthetic routes for the fabrication of Co@H-NCNT are depicted in Fig. 1a. Pristine MWCNT (0.5 g) were reacted with H_2O_2 (500 mL) at 70 $^\circ\text{C}$ for 2 days, and then annealed with urea (5.0 g) at 700 $^\circ\text{C}$ for 30 min to obtain the H-NCNT; the details of the H-NCNT synthetic routes are given in our previous study [49]. The H-NCNT (0.5 g) were dispersed in DMF (200 mL) under ultrasonication, and then $\text{CoCl}_2 \cdot 6 \text{H}_2\text{O}$ (10 g) was dissolved in the mixture. Then, the mixture was stirred for 1 day so that the DMF/ $\text{CoCl}_2 \cdot 6 \text{H}_2\text{O}$ solution permeated into the inner space of H-NCNT. Then, the mixture was filtered using a nylon filter (pore size: 0.45 μm) to collect the H-NCNT filled with DMF/ $\text{CoCl}_2 \cdot 6 \text{H}_2\text{O}$ (DMF/ $\text{CoCl}_2 \cdot 6 \text{H}_2\text{O}$ @H-NCNT). Finally, the DMF/ $\text{CoCl}_2 \cdot 6 \text{H}_2\text{O}$ @H-NCNT were annealed in a N_2 atmosphere at 500 $^\circ\text{C}$ for 1 h to fabricate Co@H-NCNT. The Fe@H-NCNT and Ni@H-NCNT were also prepared according to the procedure described above.

A mixture of Co nanoparticles and H-NCNT (Co/H-NCNT) was fabricated to compare its electrocatalytic activity with Co@H-NCNT. The H-NCNT (0.5 g) were dispersed in DMF (20 mL) under ultrasonication, and then $\text{CoCl}_2 \cdot 6 \text{H}_2\text{O}$ (0.3 g) was dissolved in the mixture. The mixture was not agitated further and immediately annealed in the N_2 atmosphere at 500 $^\circ\text{C}$ for 1 h to prevent the permeation of DMF/ $\text{CoCl}_2 \cdot 6 \text{H}_2\text{O}$ solution into the H-NCNT. The resulting Co/H-NCNT exhibited similar weight ratio of Co nanoparticles and H-NCNT with Co@H-NCNT, as shown in Fig. S1.

2.3. Characterization of catalysts

High-resolution transmission microscopy (HR-TEM, JEM-2100F, JEOL, Japan) was used to examine the morphology of all the prepared catalysts. The formation of H-NCNT and transition metal nanoparticles was confirmed using X-ray photoelectron spectroscopy (XPS, K-Alpha+, Thermo Fisher Scientific, USA) and X-ray diffraction analysis (XRD, D8-Advance, Bruker-AXS, Germany). Thermogravimetric analysis (TGA, TGA-2050, TA Instruments, USA) was performed to determine the amount of Co nanoparticles in the H-NCNT. The specific surface area of catalysts was estimated by using Brunauer-Emmett-Teller analysis (BET, 3Flex, Micromeritics, USA).

2.4. Electrochemical measurements

The catalyst paste was created by ultrasonically dispersing each catalyst (5 mg) in an aqueous solution containing Nafion (5 mL, 0.5 wt %). Subsequently, the catalyst paste (10 μL) was placed on a glassy carbon electrode (GCE, diameter: 3 mm), and then dried at 80 $^\circ\text{C}$ for 1 h. A bi-potentiostat (DY2322, Digi-Ivy, USA) with a three-electrode configuration was used for electrochemical measurements. The reference, counter, and working electrodes were the Ag/AgCl electrode, Pt wire, and the catalyst-deposited GCE, respectively.

For the ORR measurements, rotating ring disk electrode (RRDE) tests were performed in an 0.1 M KOH solution purged by O_2 . Linear sweep

voltammetry (LSV) was performed to obtain the ORR polarization curves in the potential range from 0.2 to -1.0 V with a scan rate of 10 mV/s and various rotation speeds from 400 to 2400 rpm. During the LSV measurements, the ring electrode potential was held constant at 0.8 V. The number of electrons transferred to O_2 and peroxide yield were estimated as follows:

$$n = 4 \times \frac{I_d}{I_d + I_r/N} \quad (1)$$

$$\text{HO}_2^- \% = 200 \times \frac{I_r/N}{I_d + I_r/N} \quad (2)$$

where I_d is the disk current and I_r is the ring current. N is the current collection efficiency of the Pt ring electrode (0.424). The n value was also calculated using Koutecky-Levich (K-L) equation [50]:

$$\frac{1}{J} = \frac{1}{J_L} + \frac{1}{J_k} = \frac{1}{0.201nFC_0D_0^{2/3}\nu^{-1/6}\omega^{1/2}} + \frac{1}{J_k} \quad (3)$$

where J , J_L , and J_k are the measured current density, diffusion limiting, and kinetic limiting current density, respectively. F is the Faraday constant (96,485 C/mol), C_0 is the bulk concentration of O_2 (1.2×10^{-6} mol/ cm^3), D_0 is the diffusion coefficient of O_2 in the 0.1 M KOH solution (1.9×10^{-5} cm^2/s), ν is kinetic viscosity of the solution (0.01 cm^2/s), and ω is rotation speed (rpm). For the OER measurements, the LSV was performed in the potential range from 0.2 to 1.4 V with a scan rate of 10 mV/s in an 1.0 M KOH solution purged by O_2 . Tafel slopes were calculated using the Tafel equation as follows:

$$\eta = a + b \log |J|, \quad (4)$$

where η , b , and J are the OER overpotential, Tafel slope, and current density, respectively. The double-layer capacitance (C) was obtained from the cyclic voltammetry (CV) curves in the potential range from 0 to 0.1 V in the O_2 -saturated 0.1 M KOH solution to calculate the electrochemically active surface area (ECSA) of catalysts as follows:

$$\text{ECSA} = C/C_{\text{GCE}}, \quad (5)$$

where C_{GCE} is the double-layer capacitance of the GCE (0.2 F m^{-2}).

2.5. Zn-air battery tests

The rechargeable Zn-air battery containing catalysts on the air cathode was prepared as follows. The catalyst paste (3 mL) prepared according to the procedure in Section 2.4 was placed on a carbon paper (HCP030, Alfa Aesar) with a diameter of 1 cm, and then dried at 80 $^\circ\text{C}$ for 1 h. The catalyst-loaded carbon paper was examined as the cathode of Zn-air batteries. A polished Zn plate purchased from Alfa Aesar was used as the anode of Zn-air batteries. The electrolyte was prepared by dissolving KOH (6 M) and zinc acetate (0.2 M) in the water. The performance of the Zn-air battery was explored using an electrochemical workstation (CS350, CorrTest, China).

2.6. Density function theory calculations

Electrochemical properties and catalytic activity of H-NCNT and M@H-NCNT were characterized by the DFT calculation. The Co@H-NCNT were modeled as follows: a Co nanoparticle based on six Co atoms was encapsulated in a $5 \times 5 \times 5$ armchair CNT having a hole containing nitrogen species. The simulation cell was expanded to 15 Å except for periodic regions to avoid interactions between the adjacent cells. All calculations were performed using the Quantum Espresso package [51]. Generalized gradient approximation (GGA) of Perdew-Bruke-Ernzerhof was used to describe the exchange-correlation effect [52]. A plane wave basis was employed with a kinetic cutoff energy of 30 Ry. A $3 \times 3 \times 5$ Monkhorst-Pack grid was used for the

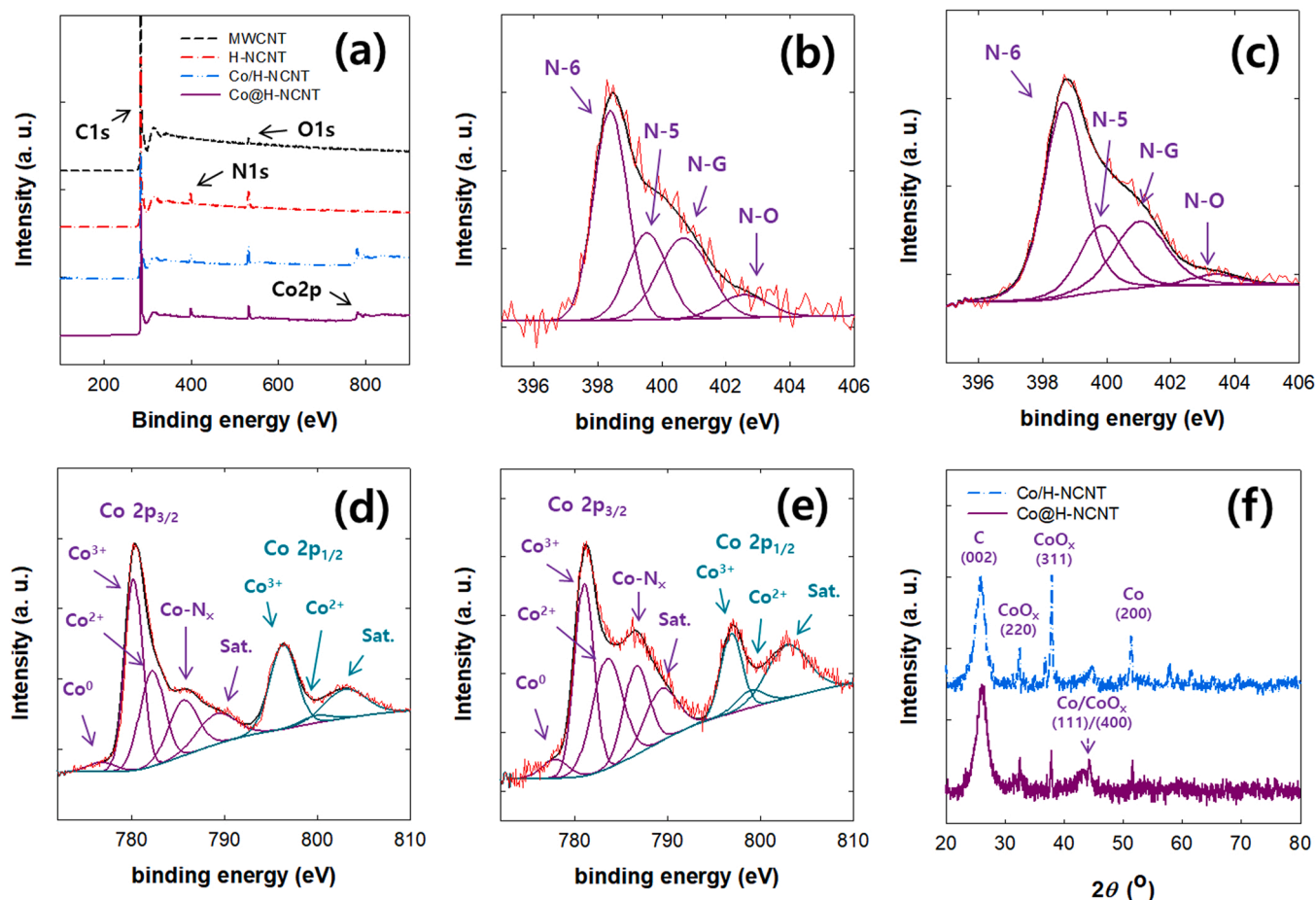


Fig. 2. (a) wide-scan XPS spectra and (b) N1s spectrum of Co/H-NCNT, (c) N1s spectrum of Co@H-NCNT, (d) Co2p spectrum of Co/H-NCNT, (e) Co2p spectrum of Co@H-NCNT, and (f) XRD patterns of Co/H-NCNT and Co@H-NCNT.

Brillouin zone samplings. The structure of Co@H-NCNT was optimized until the energy and force were converged at 10^{-8} Ry and 10^{-4} Ry/Bohr, respectively. Vibrational frequency calculation for adsorbed molecules was performed to obtain zero-point energy (ZPE) and entropy of the catalysts. The details of estimating the reaction free energies and volcano plots for ORR and OER are described in the [Supporting information](#).

Free energies of the elementary reactions for ORR and OER (Eqs. (12)–(15)) were calculated as follows:

$$\Delta G = \Delta E + \Delta ZPE - T\Delta S + \Delta G_U, \quad (6)$$

where ΔE , ZPE , and ΔS are the changes in reaction energy, zero-point energy, and entropy, respectively. $\Delta G_U = -neU$, where n is the electron transfer number of each elementary reaction, and U is the applied potential (vs. standard hydrogen electrode) and was assumed to be 0 V. The free energies of molecules in Eqs. (12)–(15) were estimated as follows.

$$G_{H_2O(l)} = G_{H_2O(g)} + RT \ln \frac{P}{P_0} \quad (7)$$

$$G_{O_2(g)} = 2G_{H_2O(l)} - 2G_{H_2(g)} + 4.92 \text{ eV} \quad (8)$$

$$G_{OH^-} = G_{H_2O(l)} - \frac{1}{2}G_{H_2(g)} + pH \times k_B T \ln 10, \quad (9)$$

where R is the ideal gas constant, $T = 298.15$ K, $p = 0.035$ bar and $p_0 = 1$ bar. $pH = 13$ for 0.1 M KOH solution and k_B is the Boltzmann constant and. $G_{H_2O(g)}$ and $G_{H_2(g)}$ were determined by DFT calculations. The

ORR and OER overpotentials used in the volcano plots were calculated as follows [53]:

$$\eta^{ORR} = \Delta G^{ORR} / e + U \quad (10)$$

$$\eta^{OER} = \Delta G^{OER} / e + U, \quad (11)$$

where ΔG^{ORR} and ΔG^{OER} of the highest reaction free energy obtained by using Eq. (10), among the elementary reactions for ORR and OER, respectively. U was assumed to be 0 V as in the free energy calculation. ΔG_{OH^-} and $\Delta G_{O^*} - \Delta G_{OH^-}$ were calculated using Eq. (10), and were used for determining the volcano plots.

3. Results and discussion

3.1. Characteristics of the Co@H-NCNT and Co/H-NCNT

Fig. 1 shows a schematic illustration for the fabrication of Co@H-NCNT. H-NCNT were fabricated by reacting MWCNT with H_2O_2 and pyrolysis with urea [49]. Then, the Co precursor solution was inserted into the inner space of H-NCNT, and annealing was done to obtain the Co@H-NCNT. The DMF/ $CoCl_2 \cdot 6H_2O$ precursor solution was chosen because it exhibited the appropriate mobility to be inserted inside the H-NCNT, whereas other solvent and precursors did not. The MWCNT with an inner diameter of 5–10 nm was used to reduce Co nanoparticle size as much as possible without hindering Co encapsulation. The Co/H-NCNT were prepared by mixing Co nanoparticles with H-NCNT for comparison with Co@H-NCNT. When the Co@H-NCNT were heated to 800 °C in air, the weight ratio of the residue was estimated to be

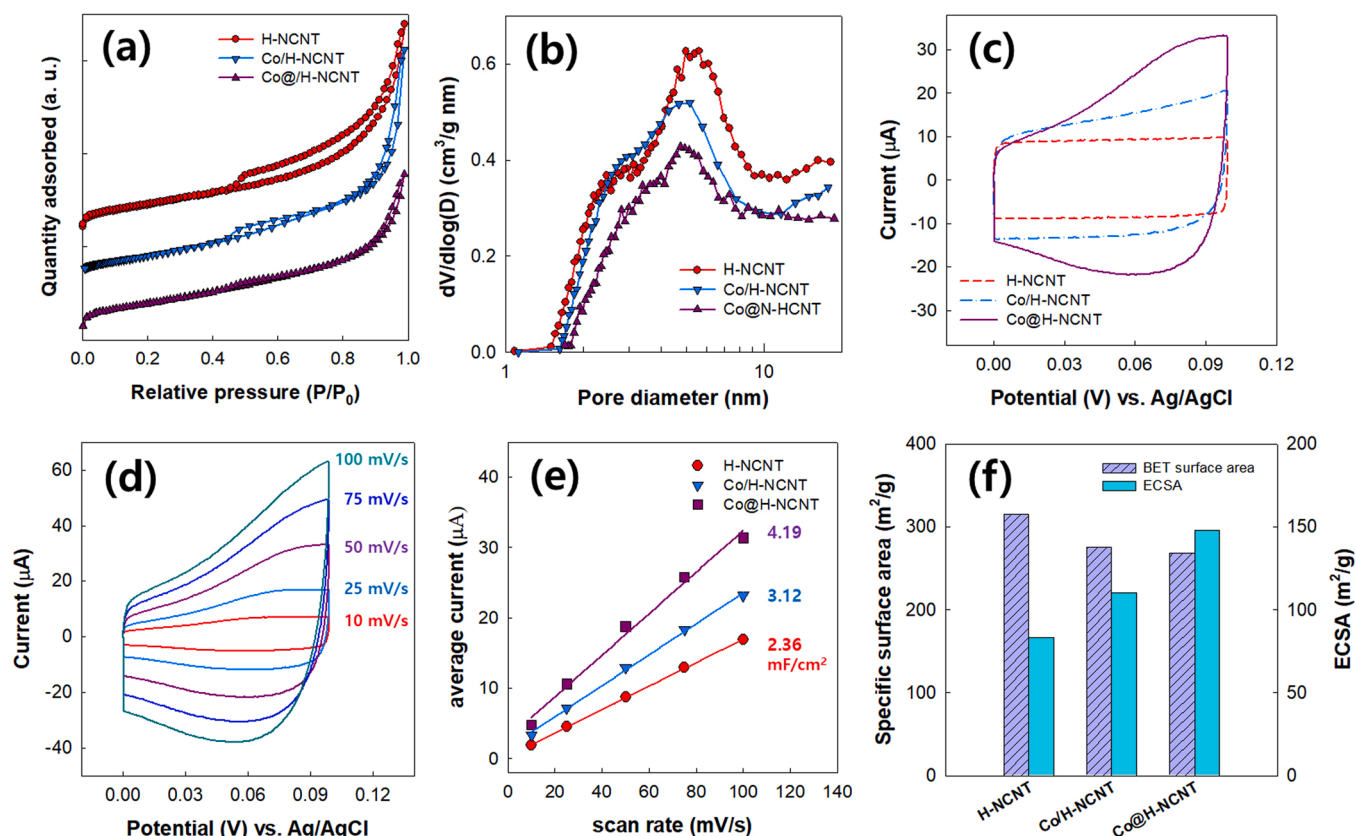


Fig. 3. (a) Nitrogen adsorption isotherms, (b) pore diameter distributions, (c) CV curves of the samples at a scan rate of 50 mV/s in 0.1 M KOH solution purged by O_2 , (d) CV curves of Co@H-NCNT at scan rates from 10 to 100 mV/s, (e) double-layer capacitance, and (f) specific surface area and ECSA of H-NCNT, Co/H-NCNT, and Co@H-NCNT.

20.4 wt% (Fig. S1). The thermal decomposition of Co@H-NCNT is due to the MWCNT that can be thermally decomposed in air [54,55], therefore, the residue is Co nanoparticles. As a result, the Co to H-NCNT ratio of the Co@H-NCNT was approximately 1:4, and the Co/H-NCNT were prepared with the same Co to H-NCNT ratio. HR-TEM images of MWCNT and H-NCNT (Figs. 1b and 1c) show that the formation of holes on the MWCNT walls after the reaction with H_2O_2 and pyrolysis with urea. The HR-TEM image of Co/H-NCNT (Fig. 1d) indicates that a large Co agglomerate was formed on the H-NCNT. In contrast, small and uniform Co nanoparticles were formed and encapsulated in the inner space of the H-NCNT (Fig. 1e). This result reveals that the Co@H-NCNT microstructure prevented Co from agglomerating and that the Co particles were distributed uniformly in the H-NCNT. Energy dispersive X-ray spectroscopy (EDS) mapping also describes the formation of N-doped species and Co nanoparticles in the Co@H-NCNT (Fig. 1f) and Co/H-NCNT (Fig. S2).

The changes in the chemical structures of the samples were assessed using XPS and XRD analyses. Fig. 2a shows the wide-scan XPS spectra, and the elemental compositions estimated from the XPS spectra are presented in Table S1. The N content of Co@H-NCNT (3.2 %) was similar to that of Co/H-NCNT (3.1 %). However, the Co@H-NCNT showed a lower Co content (1.6 %) than Co/H-NCNT (2.4 %), although Co/H-NCNT and Co@H-NCNT were prepared with a similar weight ratio of Co nanoparticles. The H-NCNT surface covers the Co nanoparticles of Co@H-NCNT; hence, Co was detected in lesser quantities for Co@H-NCNT than that for Co/H-NCNT by the XPS analysis. The N1s peaks in the XPS spectra of Co/H-NCNT and Co@H-NCNT (Figs. 2b and 2c) were split into four species, including pyridinic N (N-6), pyrrolic N (N-5), graphitic N (N-G), and oxidized N (N-O), indicating the formation of N-dopants on the H-NCNT. In the Co2p peaks of Co/H-NCNT and Co@H-NCNT (Figs. 2d and 2e), the component peaks of Co^0 ,

Co^{2+} , and Co^{3+} indicate that the nanoparticles consist of Co metal and Co oxides. This result was also described in the XRD patterns of Co/H-NCNT and Co@H-NCNT, which exhibited (111) and (200) planes corresponding to Co metal (JCPDS #15-0806), and (220), (311) and (400) planes corresponding to Co oxide (JCPDS # 42-1467). For the Co-N_x peak in the XPS spectra, Co@H-NCNT showed higher content (17.6 at%) than Co/H-NCNT (12.1 at%), although they have a similar weight ratio of Co and H-NCNT. As shown in Figs. 1d and 1e, Co agglomerates of the Co/H-NCNT partially interact with the N dopants, whereas a higher number of Co nanoparticles of Co@H-NCNT interact with the N dopants due to the uniform Co dispersion. Therefore, the Co@H-NCNT microstructure can lead to the effective formation of Co/N-C active moieties.

BET and Barrett-Joyner-Halenda (BJH) analyses were performed to investigate the surface area, pore volume, and pore size of the samples. Fig. 3a shows the N_2 gas sorption isotherms of the samples; the estimated specific surface area was decreased in the order of H-NCNT (315.3 m^2/g) > Co/H-NCNT (275.3 m^2/g) > Co@H-NCNT (268.0 m^2/g). The pore diameter distribution of the samples (Fig. 3b) exhibits that many pores of 5–6 nm developed, and the peak intensity of these pores decreased in the same order as the specific surface area of the samples. Since the pores and large surface area of H-NCNT originate from the formation of holes [49], the hybridization of Co nanoparticles with H-NCNT reduced the pore volume and specific surface area by covering the holes. Moreover, the Co@H-NCNT exhibited lower pore volume and specific surface area than the Co/H-NCNT, because encapsulating Co nanoparticles in the H-NCNT blocked holes and inner space of H-NCNT as shown in Fig. 1e. Cyclic voltammetry (CV) was performed on the samples with various scan rates (Figs. 3c and 3d) to calculate the double-layer capacitance (Fig. 3e), and consequently used to estimate the electrochemical active surface area (ECSA) of the samples (Fig. 3f). The ECSA increased as follows: H-NCNT (83.5 m^2/g) < Co/H-NCNT (110.3 m^2/g)

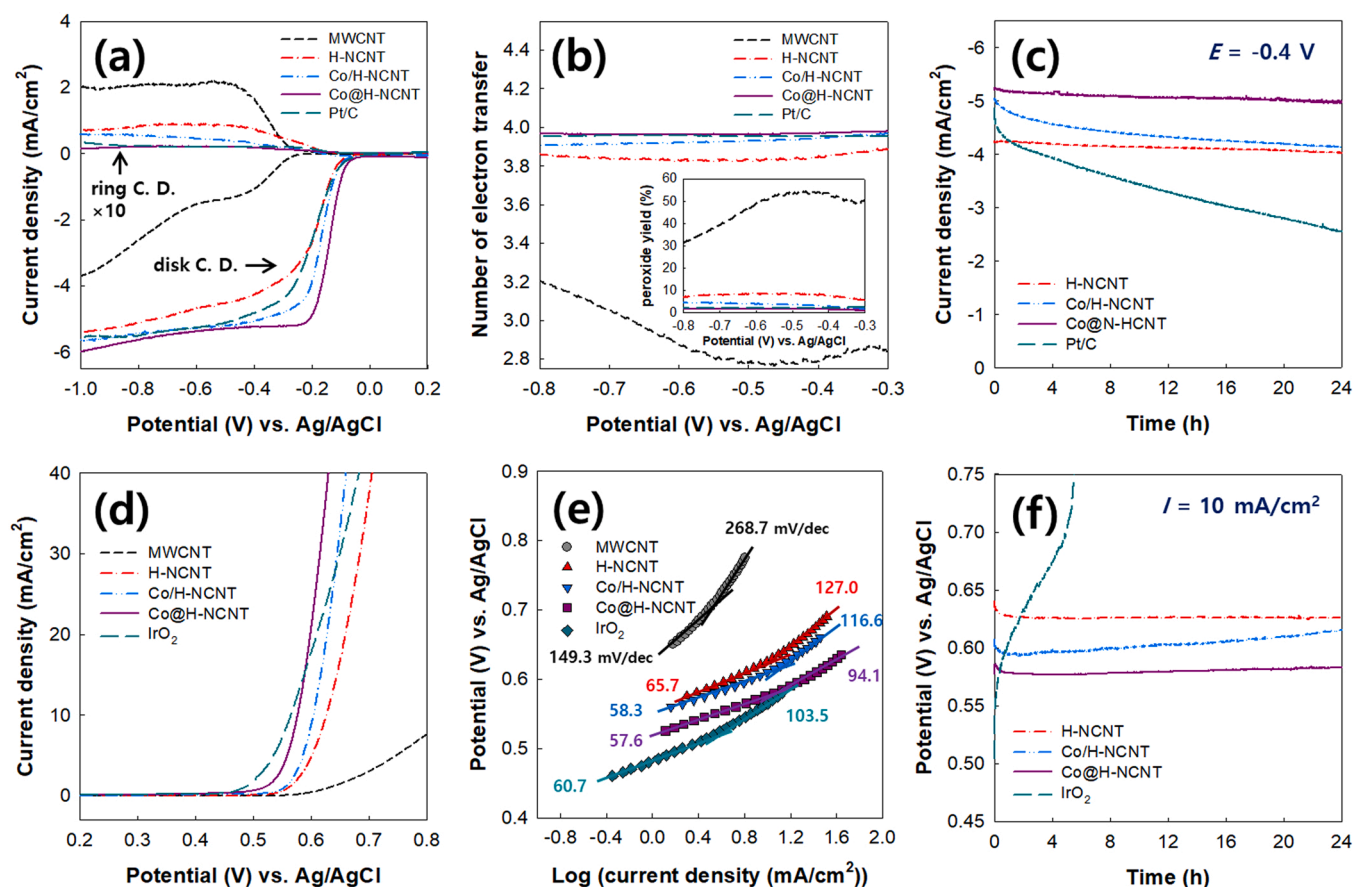


Fig. 4. (a) ORR polarization curves, (b) number of transferred electrons and peroxide yield for ORR, (c) chronoamperometric response at -0.4 V, (d) OER polarization curves, (e) Tafel plot and (f) galvanometric response at 10 mA/cm^2 of the pristine MWCNT, H-NCNT, Co/H-NCNT, Co@H-NCNT, and Pt/C or IrO₂.

< Co@H-NCNT ($148.0 \text{ m}^2/\text{g}$). The Co@H-NCNT has a higher ECSA than the Co/H-NCNT, although the Co@H-NCNT has a lower specific surface area than Co/H-NCNT. As shown in the XPS spectra (Fig. 2), the formation of the Co@H-NCNT microstructure was effective in developing Co/N-C moieties. Since the Co/N-C active site is critical for electrocatalysts to have a high active surface area [56,57], the abundant Co/N-C moieties in the Co@H-NCNT result in the high ECSA of Co@H-NCNT.

3.2. Electrocatalytic activities of the Co@H-NCNT and Co/H-NCNT

The electrocatalytic activities of the samples toward ORR and OER were investigated compared with the Pt/C and IrO₂, which have the best ORR and OER performance. Fig. 4a illustrates the ORR polarization curves of the samples obtained using the RRDE measurement. The Co@H-NCNT showed the highest ORR activity among all samples and even showed current density (-5.24 mA/cm^2 at -0.4 V) and higher onset potential (-0.08 V) than the Pt/C (-4.81 mA/cm^2 at -0.4 V and -0.10 V). The number of electrons of Co@H-NCNT transferred as calculated from the RRDE data (Fig. 4b) and Koutecky-Levich plot (Fig. S3) was almost 4.0, and the Co@H-NCNT showed a very low peroxide yield of less than 1.9%. These results suggest the efficient O₂ reduction via the four-electron pathway on the Co@H-NCNT surface. The ORR stability of the samples for 1 day of reaction was characterized by the chronoamperometric response at a constant potential (Fig. 4c). The H-NCNT showed a 5.2% decrease in the current density, whereas Pt/C showed a 47.2% decrease in the current density after 24 h of ORR. This remarkable ORR stability was also observed in other N-doped carbon materials, owing to the structural stability of N dopants in an alkaline medium [58,59]. The ORR current density of Co/H-NCNT

decreased steadily and became similar to that of H-NCNT. The decrease in catalytic activity of Co/H-NCNT toward ORR is attributed to the degradation and demetallation of Co nanoparticles during the ORR [60]. In contrast, the ORR current density of Co@H-NCNT did not change significantly. These results indicate that encapsulating Co nanoparticles in H-NCNT can effectively prevent the decrease in the catalytic activity of Co nanoparticles during ORR.

To characterize the OER activities of the samples, OER polarization curves were obtained and Tafel plots were constructed using Eq. (4), as shown in Figs. 4d and 4e. Co@H-NCNT exhibited a OER potential of 0.58 V at a current density of 10 mA/cm^2 , which was similar to that of IrO₂ (0.57 V). In addition, Tafel slope for Co@H-NCNT was the lowest among the samples and even lower than that of IrO₂, both in low overpotential (58.3 mV/sec) and high overpotential (116.6 mV/sec) ranges. This result suggests that Co@H-NCNT had the best reaction kinetics for OER in both of electron transfer and rate-determining steps. Fig. 4f exhibits the OER stability of the samples obtained from galvanometric responses at a current density of 10 mA/cm^2 . The IrO₂ showed a rapid increase in OER potential and deactivated after a few hours due to the electrolytic corrosion [61]. Similarly, with the results of the ORR stability test, the OER potential of Co@H-NCNT remained almost unchanged, whereas that of Co/H-NCNT became similar to that of H-NCNT. This result also demonstrates the advantage of Co@H-NCNT microstructure leading to high stability during the OER.

3.3. Characteristics of the Fe@H-NCNT and Ni@H-NCNT and comparison of their performance with Co@H-NCNT

Fe@H-NCNT and Ni@H-NCNT were prepared following the same procedure for the fabrication of Co@H-NCNT, and their properties and

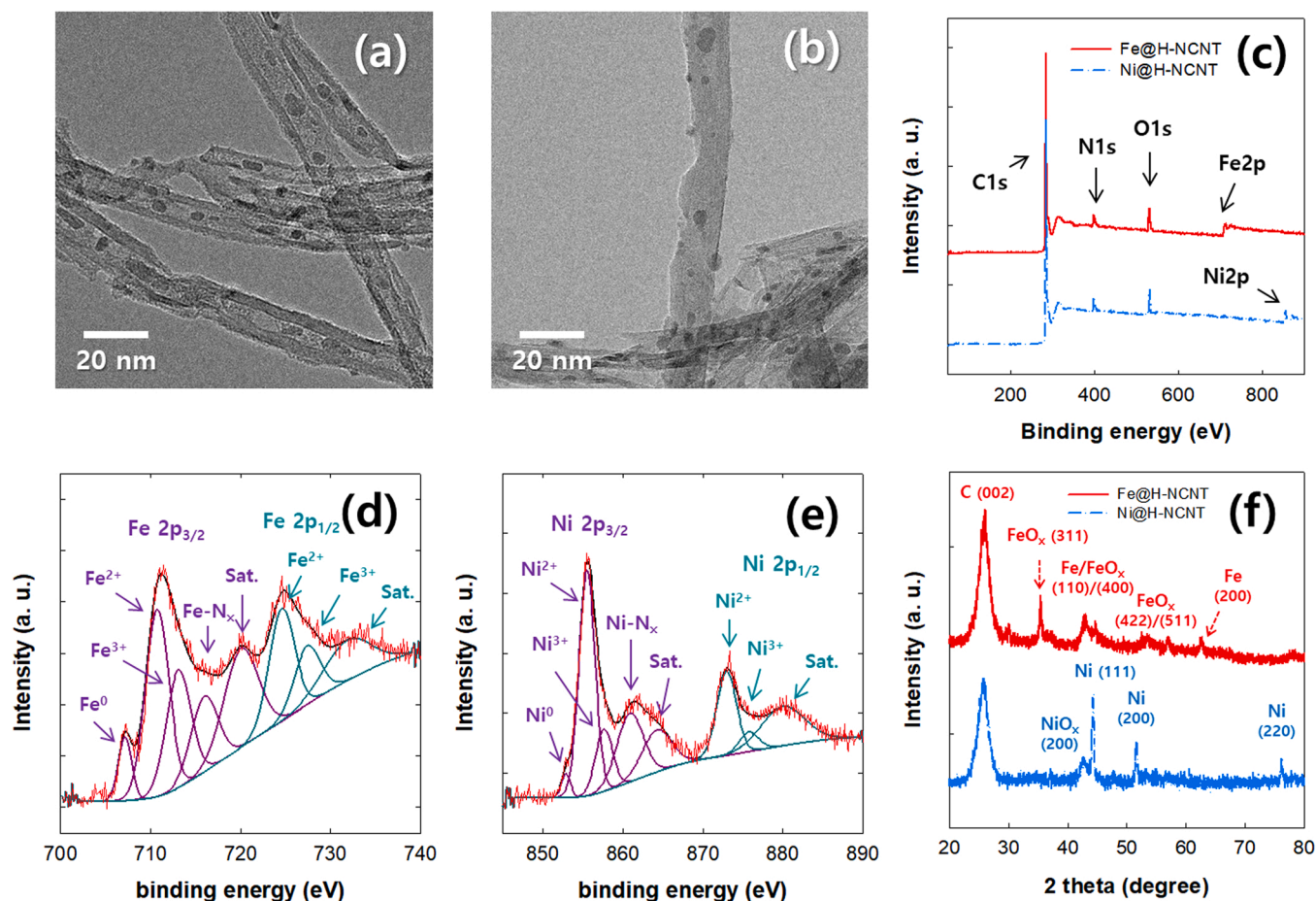


Fig. 5. HR-TEM photographs of (a) Fe@H-NCNT and (b) Ni@H-NCNT, (c) XPS spectra of Fe@H-NCNT and Ni@H-NCNT, (d) high-resolution Fe2p spectrum of Fe@H-NCNT, (e) Ni2p spectrum of Ni@H-NCNT, and (f) XRD patterns of Fe@H-NCNT and Ni@H-NCNT.

catalytic activities were characterized to compare those with Co@H-NCNT. Fig. 5a and 5b shows the HR-TEM photographs of Fe@H-NCNT and Ni@H-NCNT, respectively. EDS mapping results of Fe@H-NCNT and Ni@H-NCNT (Fig. S4) indicate that the Fe and Ni nanoparticles were successfully encapsulated in the H-NCNT. Fe and Ni species were also observed in the XPS spectra of Fe@H-NCNT and Ni@H-NCNT (Fig. 5c). The Fe2p peak of Fe@H-NCNT was split into component peaks of Fe⁰, Fe²⁺, Fe³⁺, and Fe-N_x (Fig. 5d), and the Ni2p peak of Ni@H-NCNT was deconvoluted into component peaks of Ni⁰, Ni²⁺, Ni³⁺, and Ni-N_x (Fig. 5e). These results describes that the nanoparticles comprising Fe and Ni oxide (or Ni and Ni oxide) were encapsulated in the H-NCNT, and the Fe/N-C and Ni/N-C active sites were formed on the Fe@H-NCNT and Ni@H-NCNT, respectively. The formation of Fe and Ni nanoparticles in the H-NCNT was also revealed in the XRD patterns (Fig. 5f). The XRD pattern of Fe@H-NCNT showed (110) and (200) planes corresponding to Fe metal (JCPDS #06-0696), and (311), (400) and (511) planes corresponding to Fe oxide (JCPDS #03-0863). The XRD pattern of Ni@H-NCNT showed (111), (200) and (220) planes corresponding to Ni metal (JCPDS #03-1051), and (200) plane corresponding to Ni oxide (JCPDS #47-1049). The ECSA of the Fe@H-NCNT and Ni@H-NCNT calculated from the double-layer capacitance (Fig. S5) were 116.8 m²/g and 99.8 m²/g, respectively, and were lower than that of Co@H-NCNT.

The catalytic activities of Fe@H-NCNT and Ni@H-NCNT toward ORR and OER were evaluated and compared with those of Co@H-NCNT, as shown in Fig. 6. All the prepared M@H-NCNT exhibited comparable ORR and OER performances to those of Pt/C or IrO₂. For the ORR, the Fe@H-NCNT showed better ORR activity than Ni@H-NCNT, such as higher onset potential (−0.11 V), current density at −0.4 V

(−5.01 mA/cm²), number of electrons transferred (∼3.94), and lower peroxide yield (∼3.1 %). In contrast, the Ni@H-NCNT showed better OER activity than the Fe@H-NCNT, such as lower Tafel slope and lower OER potential (0.60 V) at 10 mA/cm². The Co@H-NCNT exhibited better ORR and OER activities than both Fe@H-NCNT and Ni@H-NCNT. In summary, ORR activities were increased in the order of Ni@H-NCNT < Fe@H-NCNT < Co@H-NCNT, whereas OER activities increased in the order of Fe@H-NCNT < Ni@H-NCNT < Co@H-NCNT.

3.4. Electrocatalytic activities of the catalysts based on DFT calculations

The difference between the electrocatalytic activities of the M@H-NCNT was further characterized using the DFT. Fig. 7a shows that the M@H-NCNT structure including N-doped species, hole defect, and the metal nanoparticle was optimized, and then the catalytic activities of M-N-6, M-N-5, and M-N-G active sites were determined by the DFT calculation. There is no substantial difference in catalytic activity between N-coordinated metal and metal oxides [62], hence metal oxide was not included in the calculation model. The H-NCNT structure without the metal nanoparticle was constructed, and the catalytic activities of N-6, N-5, and N-G were explored. As illustrated in Figs. 7b and 7c, the ORR and OER overpotentials (η_{ORR} and η_{OER}) were obtained by the DFT calculation for each active site and plotted with ΔG_{OH^*} and $\Delta G_{\text{O}^*} - \Delta G_{\text{OH}^*}$ as descriptors, respectively. These volcano relationships are well established for the characterization of ORR and OER activities on metal and N-C surfaces [53,63–66]. Most M-N-6, M-N-5, and M-N-G active sites exhibited lower η_{ORR} and η_{OER} than those of N-6, N-5, and N-G, indicating that the N dopants coordinated with metals have higher ORR and OER activities than N dopants without metals. All M-N-6

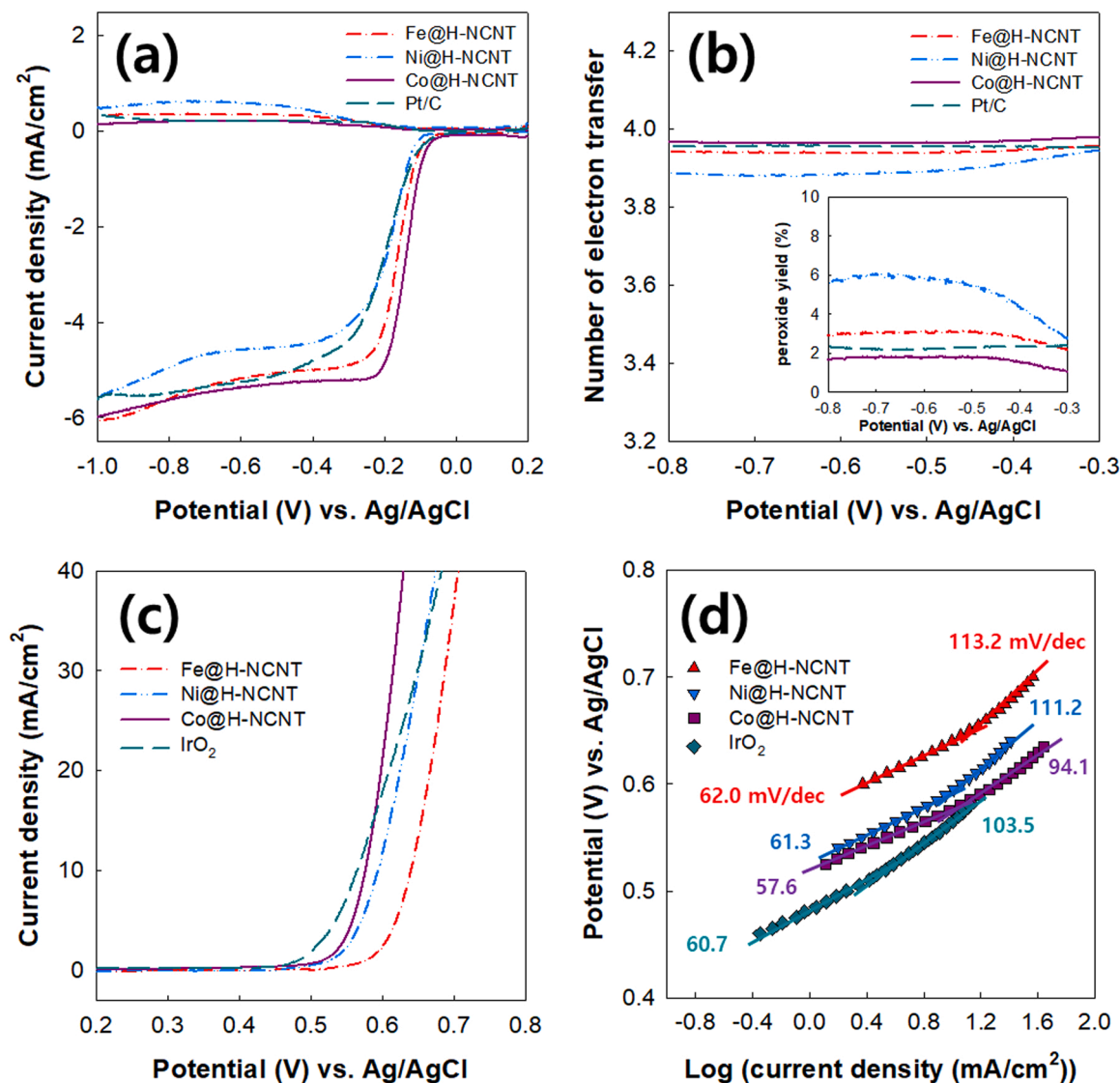
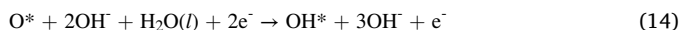
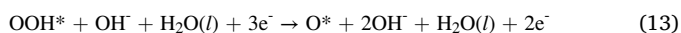
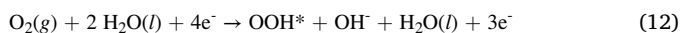


Fig. 6. (a) ORR polarization curves, (b) number of transferred electrons and peroxide yield, (c) OER polarization curves, and (d) Tafel plots of the Fe@H-NCNT, Ni@H-NCNT, Co@H-NCNT, and Pt/C or IrO₂.

exhibited lower η_{ORR} and η_{OER} than M-N-5 and M-N-G, indicating that the M-N-6-type active sites have high catalytic activities, which plays a major role in the reaction kinetics for ORR and OER [53,63,66,67].

Since the ORR and OER overpotentials originate from the reaction free energy at the rate-limiting step [53,63,66], the catalysts having low overpotentials should have low reaction free energies for oxygen electrocatalysis. In the alkaline medium, the ORR proceeds in the order of four elementary reactions as follows [68,69]:



where * denotes the adsorbed species on the catalysts. The OER proceeds in the reverse order of the above four elementary reactions. The free energies of all elementary reactions were estimated using the DFT calculation at the electrode potential of 0 V versus standard hydrogen electrode. As shown in Fig. 7d, the free energy diagram of the elementary reaction steps for ORR and OER clearly illustrates the difference between the catalytic reactivities of M@H-NCNT. The reaction

free energy at the rate-limiting step decreased in the order of Co@H-NCNT (0.25 eV) < Fe@H-NCNT (0.31 eV) < Ni@H-NCNT (0.42 eV) < H-NCNT (0.48 eV) for ORR, and in the order of Co@H-NCNT (0.64 eV) < Ni@H-NCNT (0.66 eV) < Fe@H-NCNT (0.67 eV) < H-NCNT (0.97 eV) for OER. These results demonstrate that the Co@H-NCNT has the highest ORR and OER activities among the M@H-NCNT examined, and the calculation results were consistent with the experimental results. Therefore, among the catalysts prepared, Co@H-NCNT has the most effective and fastest kinetics in ORR and OER owing to the low reaction free energy at the rate-limiting step.

3.5. Performance of the Co@H-NCNT-loaded Zn-air battery

Based on the experimental and DFT calculation results, the Co@H-NCNT is a promising candidate for electrocatalysis in Zn-air batteries due to the outstanding ORR and OER activities. As shown in Fig. 8a, rechargeable Zn-air batteries consisting of Zn-anode, electrolyte, and catalyst-loaded air-cathode were constructed, and their performances were compared. The Co@H-NCNT-loaded Zn-air battery had a high open-circuit voltage (OCV) of 1.52 V and showed high reliability in maintaining the brightness of light-emitting diodes (Fig. 8b). Fig. 8c shows the discharge curve and power density of M@H-NCNT or a Pt/C-

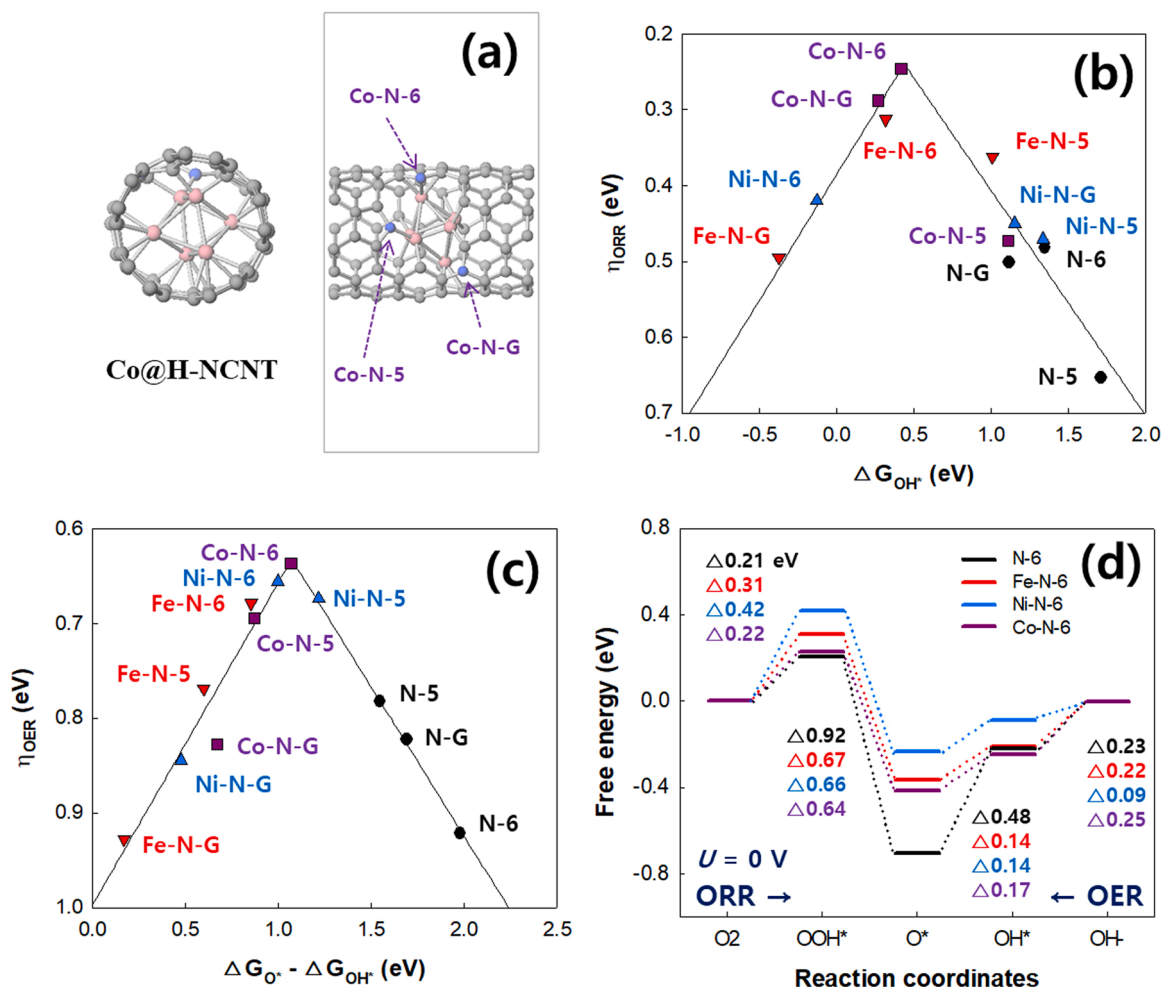


Fig. 7. (a) Atomistic model of Co@H-NCNT optimized by the DFT calculation, volcano plots of (b) ORR overpotential and (c) OER overpotential, and (d) reaction free energy diagrams of M@H-NCNT and H-NCNT.

IrO_2 composite (1:1) loaded Zn-air batteries. The Co@H-NCNT-loaded Zn-air battery showed the best discharge performance among the other samples loaded Zn-air batteries, as the peak-power density was higher in the order of Ni@H-NCNT (145.7 mW/cm^2) < Pt/C- IrO_2 composite (166.1 mW/cm^2) < Fe@H-NCNT (178.8 mW/cm^2) < Co@H-NCNT (207.0 mW/cm^2). Fig. 8d shows the galvanostatic discharge curves versus the specific capacity of Zn-air batteries characterized by normalizing the discharge current density to the amount of the consumed Zn. The Co@H-NCNT-loaded Zn-air battery showed almost no change in the discharge voltage until all Zn was consumed, and even showed a higher specific capacity than the Pt/C- IrO_2 composite-loaded Zn-air battery. The Co@H-NCNT showed outstanding charge performance in the Zn-air battery, which was comparable to the Pt/C- IrO_2 composite-loaded Zn-air battery (Fig. 8e). The long-term cycle stability of Zn-air batteries was evaluated by repeatedly performing galvanostatic charge-discharge cycling for 10 min at a current density of 10 mA/cm^2 each (Fig. 8f). After 300 cycles (100 h), the difference in charge and discharge voltages of the Co@H-NCNT-loaded Zn-air battery changed slightly from 0.71 to 0.78 V, demonstrating good cycle stability. The Co@H-NCNT-loaded Zn-air battery also exhibited good cycle stability at a different galvanostatic current density of 20 mA/cm^2 (Fig. S6). In comparison, the Pt/C- IrO_2 composite-loaded Zn-air battery exhibited less cycle stability with the difference in charge and discharge voltages changing from 0.82 to 1.07 V after 300 cycles. The performance of Pt/C- IrO_2 composite-loaded Zn-air battery after the cycle test is similar with the only Pt/C-loaded Zn-air battery [6,41], indicating that nearly all IrO_2 was deactivated due to its low OER activity. According to the

previous studies, the Zn-air batteries using other types of Co/N-C based electrocatalysts exhibited specific capacity less than 800 mAh/g [8,29, 45–48] and changes in charge-discharge voltage gap higher than 0.1 V after 300 cycles [39,42,45–48]. Therefore, using Co@H-NCNT as the electrocatalyst for Zn-air batteries has the advantages of achieving in both of high capacity and cycle stability. In summary, the Co@H-NCNT exhibited superior performance in Zn-air battery for both power density and cycle stability, making it a promising candidate for practical application in rechargeable Zn-air batteries.

4. Conclusion

Co@H-NCNT were fabricated by penetrating the precursor solution containing $\text{CoCl}_2 \cdot 6 \text{ H}_2\text{O}$ via holes of H-NCNT, followed by annealing. Co/H-NCNT were prepared by mixing Co nanoparticles with H-NCNT, and their ORR and OER activities were compared to investigate the advantages of M@N-C microstructure for electrocatalytic activity. There was no significant difference between the chemical structures of Co@H-NCNT and Co/H-NCNT; however, the ECSA of Co@H-NCNT was higher than that of Co/H-NCNT. As a result, Co@H-NCNT exhibited higher ORR and OER activities than Co/H-NCNT and even exhibited better stability in ORR and OER conditions owing to the M@N-C microstructure. Fe@H-NCNT and Ni@H-NCNT were also prepared, and their ORR and OER activities were compared with those of Co@H-NCNT. Co@H-NCNT showed the best ORR and OER performances, which even outperformed those of Pt/C and IrO_2 . The DFT calculation results revealed that Co-N-6 has the lowest ORR and OER overpotentials among the active sites

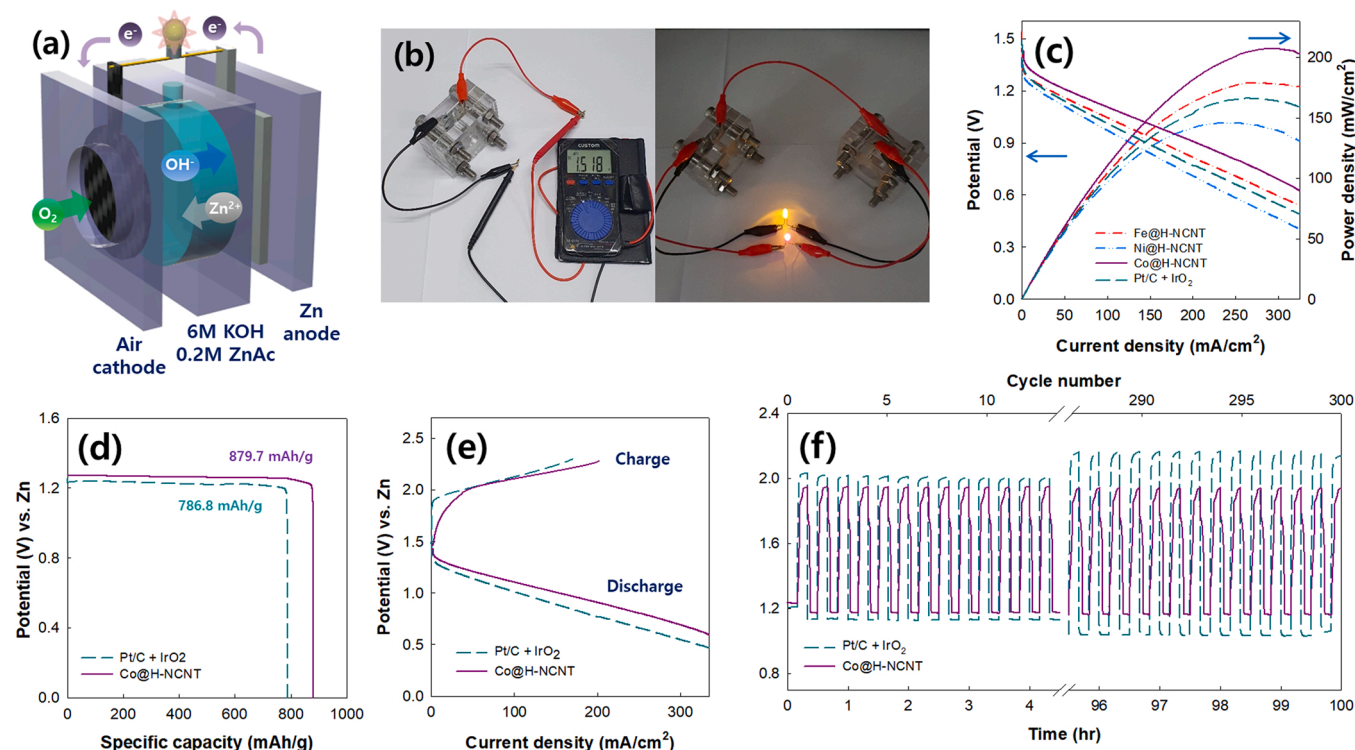


Fig. 8. (a) Schematic representation of a Zn-air battery, photographs of (b) the OCV and LED lit by the Co@H-NCNT-loaded Zn-air batteries, (c) power density and discharge curves, (d) galvanostatic discharge curves versus specific capacity, (e) discharge and charge curves, and (f) galvanostatic cycling response of catalysts loaded Zn-air batteries.

examined, resulting in the superior ORR and OER activities of Co@H-NCNT. Co@H-NCNT achieved superior performance as electrocatalysts for Zn-air batteries, exhibiting high power density, specific capacity, and long-term cycle durability. Therefore, the fabrication method of Co@H-NCNT offers novel insights to design effective electrocatalysts for ORR and OER and provides a breakthrough in the commercial application of rechargeable Zn-air batteries.

CRediT authorship contribution statement

Eun Yeop Choi: Writing – original draft, Conceptualization, Investigation, **Dong Eun Kim:** Investigation, **Seung Youn Lee:** Investigation, **Chul B. Park:** Methodology, **Chang Keun Kim:** Conceptualization, Writing – review & editing.

Declaration of Competing Interest

The authors declare the following financial interests/personal relationships which may be considered as potential competing interests: Chang Keun Kim reports financial support was provided by Chung-Ang University.

Data availability

Data will be made available on request.

Acknowledgments

This research was supported by the Chung-Ang University Research Grant in 2020.

Appendix A. Supporting information

Supplementary data associated with this article can be found in the

online version at [doi:10.1016/j.apcatb.2023.122386](https://doi.org/10.1016/j.apcatb.2023.122386).

References

- [1] P. Tan, B. Chen, H. Xu, H. Zhang, W. Cai, M. Ni, M. Liu, Z. Shao, Flexible Zn- and Li-air batteries: recent advances, challenges, and future perspectives, *Energy Environ. Sci.* 10 (2017) 2056–2080, <https://doi.org/10.1039/C7EE01913K>.
- [2] J. Pan, Y.Y. Xu, H. Yang, Z. Dong, H. Liu, B.Y. Xia, Advanced architectures and relatives of air electrodes in Zn-Air batteries, *Adv. Sci.* 5 (2018), 1700691, <https://doi.org/10.1002/advs.201700691>.
- [3] P. Tan, H.R. Jiang, X.B. Zhu, L. An, C.Y. Jung, M.C. Wu, L. Shi, W. Shyy, T.S. Zhao, Advances and challenges in lithium-air batteries, *Appl. Energy* 204 (2017) 780–806, <https://doi.org/10.1016/j.apenergy.2017.07.054>.
- [4] J. Zhang, Q. Zhou, Y. Tang, L. Zhang, Y. Li, Zinc-air batteries: are they ready for prime time, *Chem. Sci.* 10 (2019) 8924–8929, <https://doi.org/10.1039/C9SC04221K>.
- [5] P. Gu, M. Zheng, Q. Zhao, X. Xiao, H. Xue, H. Pang, Rechargeable zinc-air batteries: a promising way to green energy, *J. Mater. Chem. A* 5 (2017) 7651–7666, <https://doi.org/10.1039/C7TA01693J>.
- [6] Q. Liu, Y. Wang, L. Dia, J. Yao, Scalable fabrication of nanoporous carbon fiber films as bifunctional catalytic electrodes for flexible Zn-Air batteries, *Adv. Mater.* 28 (2016) 3000–3006, <https://doi.org/10.1002/adma.201506112>.
- [7] J. Zhang, L. Qu, G. Shi, J. Liu, J. Chen, L.N. Dai, N. P-Codoped, Carbon networks as efficient metal-free bifunctional catalysts for oxygen reduction and hydrogen evolution reactions, *Angew. Chem. Int. Ed.* 128 (2016) 2270–2274, <https://doi.org/10.1002/anie.201510495>.
- [8] H. Ge, G. Li, J. Shen, W. Ma, X. Meng, L. Xu, Co₄N nanoparticles encapsulated in N-doped carbon box as tri-functional catalyst for Zn-air battery and overall water splitting, *Appl. Cat. B: Environ.* 275 (2020), 119104, <https://doi.org/10.1016/j.apcatb.2020.119104>.
- [9] Q. Lv, N. Wang, W. Si, Z. Hou, X. Li, X. Wang, F. Zhao, Z. Yang, Y. Zhang, C. Huang, Pyridinic nitrogen exclusively doped carbon materials as efficient oxygen reduction and electrocatalysts for Zn-air batteries, *Appl. Cat. B: Environ.* 261 (2020), 118234, <https://doi.org/10.1016/j.apcatb.2019.118234>.
- [10] Y. He, W. Shang, M. Ni, Y. Huang, H. Zhao, P. Tan, In-situ observation of the gas evolution process on the air electrode of Zn-air batteries during charging, *Chem. Eng. J.* 427 (2022), 130862, <https://doi.org/10.1016/j.cej.2021.130862>.
- [11] T. Zhou, N. Zhang, C. Wu, Y. Xie, Surface/interface nanoengineering for rechargeable Zn-air batteries, *Energy Environ. Sci.* 13 (2020) 1132, <https://doi.org/10.1039/C9EE03634B>.
- [12] K.W. Leong, Y. Wang, M. Ni, W. Pan, S. Luo, D.Y.C. Leung, Rechargeable Zn-air batteries: recent trends and future perspectives, *Renew. Sustain. Energy Rev.* 154 (2022), 111771, <https://doi.org/10.1016/j.rser.2021.111771>.

- [13] J. Greeley, I.E.L. Stephens, A.S. Bondarenko, T.P. Johansson, H.A. Hansen, T. F. Jaramillo, J. Rossmeisl, I. Chorkendorff, J.K. Nørskov, Alloys of platinum and early transition metals as oxygen reduction electrocatalysts, *Nat. Chem.* 1 (2009) 552–556, <https://doi.org/10.1038/nchem.367>.
- [14] X. Zhu, X. Tan, K.H. Wu, S.C. Haw, C.W. Pao, B.J. Su, J. Jiang, S.C. Smith, J. M. Chen, R. Amal, X. Lu, Intrinsic ORR activity enhancement of Pt atomic sites by engineering the *d*-band center via local coordination tuning, *Angew. Chem. Int. Ed.* 60 (2021) 21911–21917, <https://doi.org/10.1002/anie.202107790>.
- [15] H.G.S. Casalongue, M.L. Ng, S. Kaya, D. Friebe, H. Ogasawara, A. Nilsson, In situ observation of surface species on iridium oxide nanoparticles during the oxygen evolution reaction, *Angew. Chem. Int. Ed.* 53 (2014) 7169–7172, <https://doi.org/10.1002/anie.201402311>.
- [16] D. Böhm, M. Beetz, M. Schuster, K. Peters, A.G. Hufnagel, M. Döblinger, B. Böller, T. Bein, D. Fattakhova-Rohlfing, Efficient OER catalyst with low ir volume density obtained by homogeneous deposition of iridium oxide nanoparticles on macroporous antimony-doped tin oxide support, *Adv. Funct. Mater.* 30 (2020) 1906670, <https://doi.org/10.1002/adfm.201906670>.
- [17] S. Laha, Y. Lee, F. Podjaski, D. Weber, V. Duppl, L.M. Schoop, F. Pielhofer, C. Schuerer, K. Müller, U. Starke, K. Reuter, B.V. Lotsch, Ruthenium oxide nanosheets for enhanced oxygen evolution catalysis in acidic medium, *Adv. Energy Mater.* 9 (2019) 1803795, <https://doi.org/10.1002/aenm.201803795>.
- [18] Y. Hou, Z. Wen, S. Cui, S. Ci, S. Mao, J. Chen, An advanced nitrogen-doped graphene/cobalt-embedded porous carbon polyhedron hybrid for efficient catalysis of oxygen reduction and water splitting, *Adv. Funct. Mater.* 25 (2015) 872–882, <https://doi.org/10.1002/adfm.201403657>.
- [19] W. Yang, X. Liu, X. Yue, J. Jia, S. Guo, Bamboo-like carbon nanotube/Fe₃C nanoparticle hybrids and their highly efficient catalysis for oxygen reduction, *J. Am. Chem. Soc.* 137 (2015) 1436–1439, <https://doi.org/10.1021/ja5129132>.
- [20] Y. Liu, H. Jiang, Y. Zhu, X. Yang, C. Li, Transition metals (Fe, Co, and Ni) encapsulated in nitrogen-doped carbon nanotubes as bi-functional catalysts for oxygen electrode reactions, *J. Mater. Chem. A* 4 (2016) 1694–1701, <https://doi.org/10.1039/C5TA10551J>.
- [21] G. Zhong, H. Wang, H. Yu, F. Peng, Nitrogen doped carbon nanotubes with encapsulated ferric carbide as excellent electrocatalyst for oxygen reduction reaction in acid and alkaline media, *J. Power Sources* 286 (2015) 495–503, <https://doi.org/10.1016/j.jpowsour.2015.04.021>.
- [22] J. Gautam, T.D. Thanh, K. Maiti, N.H. Kim, J.H. Lee, Highly efficient electrocatalyst of N-doped graphene-encapsulated cobalt-iron carbides towards oxygen reduction reaction, *Carbon* 137 (2018) 358–367, <https://doi.org/10.1016/j.carbon.2018.05.042>.
- [23] Y. Yang, K. Mao, S. Gao, H. Huang, G. Xia, Z. Lin, P. Jiang, C. Wang, H. Wang, Q. Chen, O-, N-atoms-coordinated mn cofactors within a graphene framework as bioinspired oxygen reduction reaction electrocatalysts, *Adv. Mater.* 30 (2018), 1801732, <https://doi.org/10.1002/adma.201801732>.
- [24] X. Liu, L. Wang, P. Yu, C. Tian, F. Sun, J. Ma, W. Li, H. Fu, A stable bifunctional catalyst for rechargeable zinc–air batteries: iron–cobalt nanoparticles embedded in a nitrogen-doped 3D carbon matrix, *Angew. Chem. Int. Ed.* 130 (2018) 16398–16402, <https://doi.org/10.1002/anie.201809009>.
- [25] L. Li, L. Song, H. Guo, W. Xia, C. Jiang, B. Gao, C. Wu, T. Wang, J. He, N-Doped porous carbon nanosheets decorated with graphitized carbon layer encapsulated Co₉S₈ nanoparticles: an efficient bifunctional electrocatalyst for the OER and ORR, *Nanoscale* 11 (2019) 901–907, <https://doi.org/10.1039/C8NR07179A>.
- [26] W.J. Niu, Y.P. Wang, J.Z. He, W.W. Liu, M.C. Liu, D. Shan, L. Lee, Y.L. Chen, Highly stable nitrogen-doped carbon nanotubes derived from carbon dots and metal-organic frameworks toward excellent efficient electrocatalyst for oxygen reduction reaction, *Nano Energy* 63 (2019), 103788, <https://doi.org/10.1016/j.nanoen.2019.05.074>.
- [27] D. Chen, J. Zhu, X. Mu, R. Cheng, W. Li, S. Liu, Z. Pu, C. Lin, S. Mu, Nitrogen-doped carbon coupled FeNi₃ intermetallic compound as advanced bifunctional electrocatalyst for OER, ORR and Zn-air batteries, *Appl. Catal. B: Environ.* 268 (2020), 118729, <https://doi.org/10.1016/j.apcatb.2020.118729>.
- [28] T. Marshall-Roth, N.J. Libretto, A.T. Wrobel, K.J. Anderton, M.L. Pegis, N.D. Rieke, T.V. Voorhis, J.T. Miller, Y. Surendranath, A pyridinic Fe–N₄ macrocycle models the active sites in Fe/N-doped carbon electrocatalysts, *Nat. Commun.* 11 (2020) 5283, <https://doi.org/10.1038/s41467-020-18969-6>.
- [29] A. Wang, C. Zhao, M. Yu, W. Wang, Trifunctional Co nanoparticle confined in defect-rich nitrogen-doped graphene for rechargeable Zn-air battery with a long lifetime, *Appl. Cat. B: Environ.* 281 (2021), 119514, <https://doi.org/10.1016/j.apcatb.2020.119514>.
- [30] C. Shi, Y. Liu, R. Qi, J. Li, J. Zhu, R. Yu, S. Li, X. Hong, J. Wu, S. Xi, L. Zhou, L. Mai, Hierarchical N-doped carbon spheres anchored with cobalt nanocrystals and single atoms for oxygen reduction reaction, *Nano Energy* 87 (2021), 106153, <https://doi.org/10.1016/j.nanoen.2021.106153>.
- [31] L. Niu, G. Liu, Y. Li, J. An, B. Zhao, J. Yang, D. Qu, X. Wang, L. An, Z. Sun, CoNi alloy nanoparticles encapsulated in N-doped graphite carbon nanotubes as an efficient electrocatalyst for oxygen reduction reaction in an alkaline medium, *ACS Sustain. Chem. Eng.* 9 (2021) 8207–8213, <https://doi.org/10.1021/acssuschemeng.1c02098>.
- [32] S. Kim, H. Yang, H. Son, H. Choi, J. Kang, O.L. Li, Near surface electric field enhancement: Pyridinic-N rich few-layer graphene encapsulating cobalt catalysts as highly active and stable bifunctional ORR/OER catalyst for seawater batteries, *Appl. Cat. B: Environ.* 310 (2022), 121361, <https://doi.org/10.1016/j.apcatb.2022.121361>.
- [33] S. Wang, H. Wang, C. Huang, P. Ye, X. Luo, J. Ning, Y. Zhong, Y. Hu, Trifunctional electrocatalyst of N-doped graphitic carbon nanosheets encapsulated with CoFe alloy nanocrystals: the key roles of bimetal components and high-content graphitic-
- N, *Appl. Cat. B: Environ.* 298 (2021), 120512, <https://doi.org/10.1016/j.apcatb.2021.120512>.
- [34] B. Liu, R. Wang, Y. Yao, J. Ma, Y. Sun, J. Wan, Y. Zhang, S. Wang, J. Zou, Hollow-structured CoP nanotubes wrapped by N-doped carbon layer with interfacial charges polarization for efficiently boosting oxygen reduction/evolution reactions, *Chem. Eng. J.* 431 (2022), 133238, <https://doi.org/10.1016/j.cej.2021.133238>.
- [35] P. Su, W. Huang, J. Zhang, U. Guharoy, Q. Du, Q. Sun, Q. Jiang, Y. Cheng, J. Yang, X. Zhang, Y. Liu, S.P. Jiang, J. Liu, Fe atoms anchored on defective nitrogen doped hollow carbon spheres as efficient electrocatalysts for oxygen reduction reaction, *Nano Res.* 14 (2021) 1069–1077, <https://doi.org/10.1007/s12274-020-3151-8>.
- [36] D. Xie, D. Yu, Y. Hao, S. Han, G. Li, X. Wu, F. Wu, L. Li, H.Y. Chen, Y.F. Liao, S. Peng, Dual-active sites engineering of N-doped hollow carbon nanocubes confining bimetal alloys as bifunctional oxygen electrocatalysts for flexible metal–air batteries, *Small* 17 (2021), 2007239, <https://doi.org/10.1002/sml.202007239>.
- [37] A. Kumar, A. Sethi, R.M. Lawrence, V.M. Dhavale, Co–Co₃O₄ nanostructure with nitrogen-doped carbon as bifunctional catalyst for oxygen electrocatalysis, *Int. J. Hydrog. Energy* 298 (2021), 120512, <https://doi.org/10.1016/j.ijhydene.2021.08.047>.
- [38] X.Z. Fan, X. Du, Q.Q. Pang, S. Zhang, Z.Y. Liu, X.Z. Yue, *In Situ* construction of bifunctional N-doped carbon-anchored Co nanoparticles for OER and ORR, *ACS Appl. Mater. Interfaces* 14 (2022) 8549–8556, <https://doi.org/10.1021/acsaami.1c21445>.
- [39] V. Jose, H. Hu, E. Edison, W. Manalastas Jr, H. Ren, P. Kidkhunthod, S. Sreejith, A. Jayakumar, J.M.V. Nsanizimana, M. Srinivasan, J. Choi, J.M. Lee, Modulation of single atomic Co and Fe sites on hollow carbon nanospheres as oxygen electrodes for rechargeable Zn-air batteries, *Small Methods* 5 (2021), 2000751, <https://doi.org/10.1002/smt.202000751>.
- [40] V. Jose, J.M.V. Nsanizimana, H. Hu, J. Choi, X. Wang, J.M. Lee, Highly efficient oxygen reduction activity of N-doped carbon-cobalt boride heterointerfaces, *Adv. Energy Mater.* 11 (2021), 2100157, <https://doi.org/10.1002/aenm.202100157>.
- [41] H.X. Zhong, K. Li, Q. Zhang, J. Wang, F.L. Meng, Z.J. Wu, J.M. Yan, X.B. Zhang, In situ anchoring of Co₉S₈ nanoparticles on N and S co-doped porous carbon tube as bifunctional oxygen electrocatalysts, *NPG Asia Mater.* 8 (2016), e308, <https://doi.org/10.1038/am.2016.132>.
- [42] Q. Lu, H. Wu, X. Zheng, Y. Chen, A.L. Rogach, X. Han, Y. Deng, W. Hu, Encapsulating cobalt nanoparticles in interconnected N-doped hollow carbon nanofibers with enriched Co–N–C moiety for enhanced oxygen electrocatalysis in Zn-air batteries, *Adv. Sci.* 8 (2021), 2101438, <https://doi.org/10.1002/advs.202101438>.
- [43] H. Wang, J. Li, K. Le, Y. Lin, J. Chen, L. Gao, V. Nicolosi, X. Xiao, J.M. Lee, Transition metal nitrides for electrochemical energy applications, *Chem. Soc. Rev.* 50 (2021) 1354–1390, <https://doi.org/10.1039/D0CS00415D>.
- [44] G. Fu, Y. Wang, Y. Tang, K. Zhou, J.B. Goodenough, J.M. Lee, Superior oxygen electrocatalysis on nickel indium thiospinels for rechargeable Zn-air batteries, *ACS Mater. Lett.* 1 (2019) 123–131, <https://doi.org/10.1021/acsmaterlett.9b00093>.
- [45] C. Tang, B. Wang, H.F. Wang, Q. Zhang, Defect engineering toward atomic Co–N_xC in hierarchical graphene for rechargeable flexible solid Zn-air batteries, *Adv. Mater.* 29 (2017), 1703185, <https://doi.org/10.1002/adma.201703185>.
- [46] Z. Wang, C. Zhu, H. Tan, J. Liu, L. Xu, Y. Zhang, Y. Liu, X. Zou, Z. Liu, X. Lu, Understanding the synergistic effects of cobalt single atoms and small nanoparticles: enhancing oxygen reduction reaction catalytic activity and stability for zinc-air batteries, *Adv. Funct. Mater.* 31 (2021), 2104735, <https://doi.org/10.1002/adfm.202104735>.
- [47] K. Chen, S. Kim, M. Je, H. Choi, Z. Shi, N. Vladimir, K.H. Kim, O.L. Li, Ultrasonic plasma engineering toward facile synthesis of single-atom M–N₄/N-doped carbon (M=Fe, Co) as superior oxygen electrocatalyst in rechargeable zinc-air batteries, *Nano-Micro Lett.* 13 (2021) 60, <https://doi.org/10.1007/s40820-020-00581-4>.
- [48] L. Wang, Z. Xu, T. Peng, M. Liu, L. Zhang, J. Zhang, Bifunctional single-atom cobalt electrocatalysts with dense active sites prepared via a silica xerogel strategy for rechargeable zinc-air batteries, *Nanomaterials* 12 (2022) 381, <https://doi.org/10.3390/nano12030381>.
- [49] E.Y. Choi, D.E. Kim, S.Y. Lee, C.K. Kim, Electrocatalytic activity of nitrogen-doped holey carbon nanotubes in oxygen reduction and evolution reactions and their application in rechargeable zinc–air batteries, *Carbon* 166 (2020) 245–255, <https://doi.org/10.1016/j.carbon.2020.05.034>.
- [50] A.J. Bard, L.R. Faulkner, *Electrochemical Methods: Fundamentals and Applications*, second ed., Wiley, New York, 2001.
- [51] P. Giannozzi, S. Baroni, N. Bonini, M. Calandra, R. Car, C. Cavazzoni, D. Ceresoli, G.L. Chiarotti, M. Cococcioni, I. Dabo, A.D. Corso, S. Gironcoli, S. Fabris, G. Fratesi, R. Gebauer, U. Gerstmann, C. Gougousis, A. Kokalj, M. Lazzeri, L. Martin-Samos, N. Marzari, F. Mauri, R. Mazzarello, S. Paolini, A. Pasquarello, L. Paulatto, C. Sbraccia, S. Scandolo, G. Sclauzero, A.P. Seitsonen, A. Smogunov, P. Umari, R. M. Wentzcovitch, QUANTUM ESPRESSO: a modular and open-source software project for quantum simulations of materials, *J. Phys. -Condens. Matter* 21 (2009), 395502, <https://doi.org/10.1088/0953-8984/21/39/395502>.
- [52] J.P. Perdew, K. Burke, M. Ernzerhof, Generalized gradient approximation made simple, *Phys. Rev. Lett.* 77 (1996) 3865, <https://doi.org/10.1103/PhysRevLett.77.3865>.
- [53] S. Zhou, X. Yang, W. Pei, N. Liu, J. Zhao, Heterostructures of MXenes and N-doped graphene as highly active bifunctional electrocatalysts, *Nanoscale* 10 (2018), <https://doi.org/10.1039/C8NR01090K>.
- [54] L.S.K. Pang, J.D. Saxby, S.P. Chatfield, Thermogravimetric analysis of carbon nanotubes and nanoparticles, *J. Phys. Chem.* 97 (1993) 6941–6942, <https://doi.org/10.1021/j100129a001>.

- [55] Y.C. Hsieh, Y.C. Chou, C.P. Lin, T.F. Hsieh, C.M. Shu, Thermal analysis of multi-walled carbon nanotubes by Kissinger's corrected kinetic equation, *Aerosol Air Qual. Res.* 10 (2010) 212–218, <https://doi.org/10.4209/aaqr.2009.08.0053>.
- [56] K. Im, D. Kim, J.H. Jang, J. Kim, S.J. Yoo, Hollow-sphere Co-NC synthesis by incorporation of ultrasonic spray pyrolysis and pseudomorphic replication and its enhanced activity toward oxygen reduction reaction, *Appl. Catal. B: Environ.* 260 (2020), 118192, <https://doi.org/10.1016/j.apcatb.2019.118192>.
- [57] Y.J. Sa, S.O. Park, G.Y. Jung, T.J. Shin, H.Y. Jeong, S.K. Kwak, S.H. Joo, Heterogeneous Co–N/C electrocatalysts with controlled cobalt site densities for the hydrogen evolution reaction: structure–activity correlations and kinetic insights, *ACS Catal.* 9 (2019) 83–97, <https://doi.org/10.1021/acscatal.8b03446>.
- [58] M. Yang, L. Wang, M. Li, T. Hou, Y. Li, Structural stability and O₂ dissociation on nitrogen-doped graphene with transition metal atoms embedded: a first-principles study, *AIP Adv.* 5 (2015), 067136, <https://doi.org/10.1063/1.4922841>.
- [59] J. Quilez-Bermejo, E. Morallón, D. Cazorla-Amorós, On the deactivation of N-doped carbon materials active sites during oxygen reduction reaction, *Carbon* 189 (2022) 548–560, <https://doi.org/10.1016/j.carbon.2021.12.086>.
- [60] C. Miry, E. Ngameni, F. Gloaguen, M. L'Her, Why Cobalt macrocyclic complexes are not efficient catalysts for the oxygen reduction reaction, under acidic conditions, *Electrochim. Acta* 358 (2020), 136854, <https://doi.org/10.1016/j.electacta.2020.136854>.
- [61] X. Tan, J. Shen, N. Semagina, M. Secanell, Decoupling structure-sensitive deactivation mechanisms of Ir/IrO_x electrocatalysts toward oxygen evolution reaction, *J. Catal.* 371 (2019) 57–70, <https://doi.org/10.1016/j.jcat.2019.01.018>.
- [62] A. Cho, B.J. Park, J.W. Han, Computational screening of single-metal-atom embedded graphene-based electrocatalysts stabilized by heteroatoms, *Front. Chem.* 10 (2022), 873609, <https://doi.org/10.3389/fchem.2022.873609>.
- [63] W. Liang, J. Chen, Y. Liu, S. Chen, Density-functional-theory calculation analysis of active sites for four-electron reduction of O₂ on Fe/N-doped graphene, *ACS Catal.* 4 (2014) 4170–4177, <https://doi.org/10.1021/cs501170a>.
- [64] S. Wannakao, T. Maihom, K. Kongpatpanich, J. Limtrakul, V. Promarak, Halogen substitutions leading to enhanced oxygen evolution and oxygen reduction reactions in metalloporphyrin frameworks, *Phys. Chem. Chem. Phys.* 19 (2017) 29540–29548, <https://doi.org/10.1039/C7CP06187K>.
- [65] Z.W. Seh, J. Kibsgaard, C.F. Dickens, I. Chorkendorff, J.K. Nørskov, T.F. Jaramillo, Combining theory and experiment in electrocatalysis: Insights into materials design, *Science* 355 (2017) 6321, <https://doi.org/10.1126/science.aad4998>.
- [66] R. Ma, G. Lin, Y. Zhou, Q. Liu, T. Zhang, G. Shan, M. Yang, J. Wang, A review of oxygen reduction mechanisms for metal-free carbon-based electrocatalysts, *Npj Comput. Mater.* 5 (2019) 78, <https://doi.org/10.1038/s41524-019-0210-3>.
- [67] X.R. Wang, J.Y. Liu, Z.W. Liu, W.C. Wang, J. Luo, X.P. Han, X.W. Du, S.Z. Qiao, J. Yang, Identifying the key role of pyridinic-N–Co bonding in synergistic electrocatalysis for reversible ORR/OER, *Adv. Mater.* 30 (2018), 1800005, <https://doi.org/10.1002/adma.201800005>.
- [68] Y. Jiao, Y. Zheng, M. Jaroniec, S.Z. Qiao, Origin of the electrocatalytic oxygen reduction activity of graphene-based catalysts: a roadmap to achieve the best performance, *J. Am. Chem. Soc.* 136 (2014) 4394–4403, <https://doi.org/10.1021/ja500432h>.
- [69] Q. Lv, W. Si, J. He, L. Sun, G. Zhang, N. Wang, Z. Yang, X. Li, X. Wang, W. Deng, Y. Long, C. Huang, Y. Li, Selectively nitrogen-doped carbon materials as superior metal-free catalysts for oxygen reduction, *Nat. Commun.* 9 (2018) 3376, <https://doi.org/10.1038/s41467-018-05878-y>.